International Journal of Pharmaceutics 634 (2023) 122669

Contents lists available at ScienceDirect

International Journal of Pharmaceutics

journal homepage: www.elsevier.com/locate/ijpharm

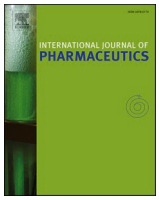

Design and development of polydioxanone scaffolds for skin tissue engineering manufactured via green process

Dalila Miele [a], Cristian Nomicisio [a], Giorgio Musitelli [a], Cinzia Boselli [a], Antonia Icaro Cornaglia [b], Rita Sànchez-Espejo [c], Barbara Vigani [a], Cesar Viseras [c], Silvia Rossi [a], Giuseppina Sandri [a,*]

[a] Department of Drug Sciences, University of Pavia, Viale Taramelli 12, 27100 Pavia, Italy
[b] Department of Public Health, Experimental and Forensic Medicine, University of Pavia, via Forlanini 2, 27100 Pavia, Italy
[c] Department of Pharmacy and Pharmaceutical Technology, Faculty of Pharmacy, University of Granada, Campus of Cartuja s/n, Granada 18071, Spain

ARTICLE INFO

Keywords:
Polydioxanone
Centrifugal spinning
Deep eutectic solvents
Preclinical in vitro and in vivo models
tissue engineering

ABSTRACT

Fiber spinning technologies attracted a great interest since the beginning of the last century. Among these, electrospinning is a widely diffuse technique; however, it presents some drawbacks such as low fiber yield, high energy demand and the use of organic solvents. On the contrary, centrifugal spinning is a more sustainable method and allows to obtain fiber using centrifugal force and melted materials. The aim of the present work was the design and the development of polydioxanone (PDO) microfibers intended for tissue engineering, using centrifugal spinning. PDO, a bioresorbable polymer currently used for sutures, was selected as low melting polyester and DES (deep eutectic solvents), either choline chloride/citric acid (ChCl/CA) or betaine/citric acid (Bet/CA) 1:1 M ratio, were used to improve PDO spinnability. Physical mixtures of DES and PDO were prepared using different weight ratios. These were then poured into the spinneret and melted at 140 °C for 5 min. After the complete melting, the blends were spun for 1 min at 700 rpm. The fibers were characterized for physico chemical properties (morphology; dimensions; chemical structure; thermal behavior; mechanical properties). Moreover, the preclinical investigation was performed in vitro (biocompatibility, adhesion and proliferation of fibroblasts) and in vivo (murine burn/excisional model to assess safety and efficacy). The multidisciplinary approach allowed to obtain an extensive characterization to develop PDO based microfibers as medical device for implant to treat full thickness skin wounds.

1. Introduction

The skin is the protective barrier against external agents (microorganisms, ultraviolet light, physical insults) and allows thermoregulation (Enoch and Leaper, 2008). The loss of its structural and functional integrity exposes the organism to issues of different origins. Usually, skin wounds rapidly heal following a complex process based on four stages (hemostasis, inflammation, proliferation, and remodeling) to restore skin integrity (Ruggeri et al., 2021; Mofazzal Jahromi et al., 2018; Ruggeri et al., 2020). However, when the healing is impaired, chronic wounds occur with a healing time greater than 12 weeks. It happens especially when there are underlining metabolic disorders (such as diabetes) and in the elderly population, mainly in the case of circulatory failure (Wilkinson and Hardman, 2020). Wound chronicization is deeply related to the inflammatory reactions which lead to the overexpression of proinflammatory cytokines, proteases, and reactive oxygen species (ROS). In this frame, the presence of senescent cells is substantial, and there is the simultaneous deficiency of stem cells. Moreover, the wound infection, common in chronic lesions, further enhances the inflammatory phase and prolongs the healing time (Frykberg and Banks, 2015). In addition, the scarring process could deserve severe issues caused by the lack of functionality of the area and its poor elasticity, which could inhibit movements, especially in the limb region. Currently there are options from tissue engineering aiming at repairing and restoring skin chronic lesions. Among these, 3D biomimetic constructs are scaffolds that act as template to enhance cell attachment, proliferation, extracellular matrix (ECM) production and deposition, thanks to their 3D structure, their porosity, their chemical, physical, and mechanical

* Corresponding author.
E-mail address: g.sandri@unipv.it (G. Sandri).

https://doi.org/10.1016/j.ijpharm.2023.122669
Received 19 August 2022; Received in revised form 21 January 2023; Accepted 28 January 2023
Available online 1 February 2023

properties (Nikolova and Chavali (2019); Chouhan et al., 2019; Kim et al., 2019).

Currently there are many examples of biomaterials-based scaffolds in skin wound healing and their mechanical properties proved to be an essential characteristic for clinical translation. Although this is controversial, the microstructure is a crucial factor not only to achieve mechanical resistance to the stress but also to positively affect the biological response of the surrounding tissue. This is conceivably due to the ECM composition made of fibers of different sizes, from nano-to micron-scale. It is reported that 350–1100 nm fiber diameters upregulate the expression of the type-III collagen gene and there is a critical minimum fiber diameter, namely 970 nm, that efficiently promote skin tissue regeneration and remodeling. Moreover, it seems that small diameter fibers (about 250–300 nm) are support stronger than bigger fibers to enhance dermal fibroblast proliferation and stem cell differentiation (Wang et al., 2022). Despite these findings, more recently there are evidences that microfibers possess superior properties in skin wound healing (Huang et al., 2022; Jia et al., 2021).

Along mechanical strength and healing enhancement, the in vivo degradation is another key point and should occur simultaneously to the formation of the ECM driven by in situ proliferating cells (Ruggeri et al., 2020; Sandri et al., 2019). Polydioxanone (PDO), a biodegradable polyester, is an interesting candidate to design 3D constructs thanks to its compatibility, degradation rate, and mechanical properties (including high elasticity and shape memory) and has been recently considered as biomaterial in tissue engineering (Boland et al., 2005). PDO scaffolds are generally characterized by mechanical properties comparable to the major structural components of native ECM, in particular, collagen and elastin (Goonoo et al., 2015). PDO is reported in literature as nonantigenic compound, capable to induce minimal tissue reaction during absorption after implantation. It is degraded by hydrolysis and is completely metabolized in the body, with an intermediate absorption duration (typically 6–8 months), particularly suitable to sustain soft tissue reparation (Martins et al., 2020).

The literature reports PDO scaffolds manufactured via electrospinning or co-electrospinning (Saska et al., 2021; Zhou et al., 2019; Boland et al., 2005; Song et al., 2018; Chaim et al., 2012; McClure et al., 2009). Nevertheless, the processes require organic solvents (such as hexafluoro propanol) to obtain electrospun nanofibers (Rashid et al., 2020), due to the PDO poor solubility properties. Moreover, electrospinning has critical issues because of low fiber yield, high energy demand and the usage of organic solvent (Rashid et al., 2020). Considering the relatively low PDO melting point (110 °C), compared to the other polyesters, centrifugal spinning of melted polymers seems the more suitable spinning technique since it avoids solvents, and allows high yields with shorter manufacturing time. The origin of this technique is traced back to the beginning of the 20th century, but the method was recently rediscovered in the 2009 (Obregon et al., 2016) when a rotating centrifuge was patented for the manufacturing of polymer fibers in the molten or liquid state.

Given these premises the aim of the work was the design and the development of novel 3D scaffolds intended as skin substitutes to be grafted in a full thickness skin wound to restore tissue integrity. These were based on microfibers made of PDO blended to a deep eutectic solvent (DES) to increase its spinnability. The plasticizing effect of DES enabled to spin melted PDO using a centrifugal spinning as innovative approach. Microfibers were selected as target to take advantage of the superior mechanical properties and the enhancement of ECM synthesis from fibroblasts driven by 3D scaffold network.

2. Experimental part

2.1. Materials

Polymer: polydioxanone (PDO, Resomer X206S, Evonik Operations GmbH, Darmstadt, Germany) 2.0 dl/g inherent viscosity.

Components of deep eutectic solvents (DES): betaine (Bet), choline chloride (ChCl) (Sigma-Aldrich, Milan, Italy), citric acid monohydrate (VWR Chemicals, Milan, Italy).

2.2. Methods

2.2.1. Fiber manufacturing

The fibers were manufactured using a customized force spinning equipment (Fig. 1), equipped with an AC motor (230 V, 50 Hz and 1030 W), a rotator system consisting of an aluminum spinneret coupled with brass needles (Ø=1 mm), a speed controller, a temperature controller coupled with a platinum sensor thermometer (PT-100) and a digital thermometer (from 20 to 300 °C). Finally, a static collector based on vertical steel bars was installed on the rotor system. PDO was spun alone or in mixture with DES. DES physical mixtures were obtained by blending betaine (Bet) or choline chloride (CHCl) to citric acid (CA) at 1:1 M ratio giving Bet/CA and CHCl/CA (Dai et al., 2013; Florindo et al., 2019). Then, PDO was added to the mixtures at different weight ratios, as reported in Table 1.

Each resultant physical mixture was poured in the spinneret and heated at 140 °C ± 10 °C for 10 min up to complete melting. Then, three 1 min spinning cycles were performed at 700 rpm. Each cycle was spaced out by 2 min time-lag to restore the initial temperature (140 ± 10 °C). The yield (Y) of the spinning process was calculated as follows:

$$\%Y = (m_f/m_p)*100$$

m_f = amount of spun fibers (mf); m_p = total mass of the physical mixture in the spinneret.

2.2.2. Physical-chemical characterization

Fiber morphology was assessed by means of scanning electron microscopy (SEM-EDS, Tescan, Mira3XMU, Brno, Czechoslovakia - ARVEDI, CISRIC, University of Pavia, I). The samples were sputtered by means of the vacuum deposition of graphite (2×10^{-4} mbar). The image acquisition was performed at high voltage (8 kV) and high vacuum (6×10^{-4} mbar) at room temperature. The representative images were acquired at different magnifications (1kx, 2kx and 5kx). Fiber morphology was then acquired also upon hydration. To this purpose fibers were dipped in pH 7.4 PBS (phosphate buffer solution, Sigma Aldrich, Milan, Italy) for 7 days at 37 °C. SEM analysis was then performed after fiber drying. The fiber diameter before and after hydration was measured using an image analysis software (Diameter plugin, Image J, NIH).

The stability of the components to the centrifugal spinning process was assessed using nuclear magnetic resonance spectroscopy (NMR). The NMR spectra were recorded at 298 K on a AVIII 400 MHz Bruker NMR spectrometer (Bruker Corporation, Billerica, MA, USA). All 1D and 2D NMR spectra were acquired using the standard pulse sequences available with Bruker Topspin 3.6. $CDCl_3$ (Merck, Milan, Italy) and DMSO-d_6 (Sigma Aldrich, Milan, Italy) and their mixture were used as solvents. Chemical shifts (δ) were expressed in ppm and referred to the solvent signal (δH 7.28 ppm for CDCl and 2.50 ppm for DMSO-d_6).

Differential scanning calorimetry (DSC) and thermogravimetric analysis (TGA) were performed by means of a TGA/DSC1 equipment (Mettler-Toledo GMBH, Spain) equipped with a microbalance (precision 0.1 μg) and with a horizontal oven, in 25–950 °C temperature range and 10 °C/min heating rate, and in atmospheric air. Approximately 20 mg of each sample were weighted in aluminum sample pans. The weight loss % has been calculated considering the % ratio between the weight loss and the initial weight.

The surface area was measured according to the Brunauer, Emmett and Teller (BET) single point (Flowsorb II 2300, Micromeritics, US). Each sample was accurately weighed (about 0.4 g) and degassed at 60 °C for 3 h under a continuous stream of a N_2:He, 30:70 mixture. Gas adsorption was then achieved by placing the sample in liquid N_2. Specific surface area (SSA) was calculated as follows (Chen et al., 2009):

SSA: surface area (m^2/g)/volume (m^3/g).

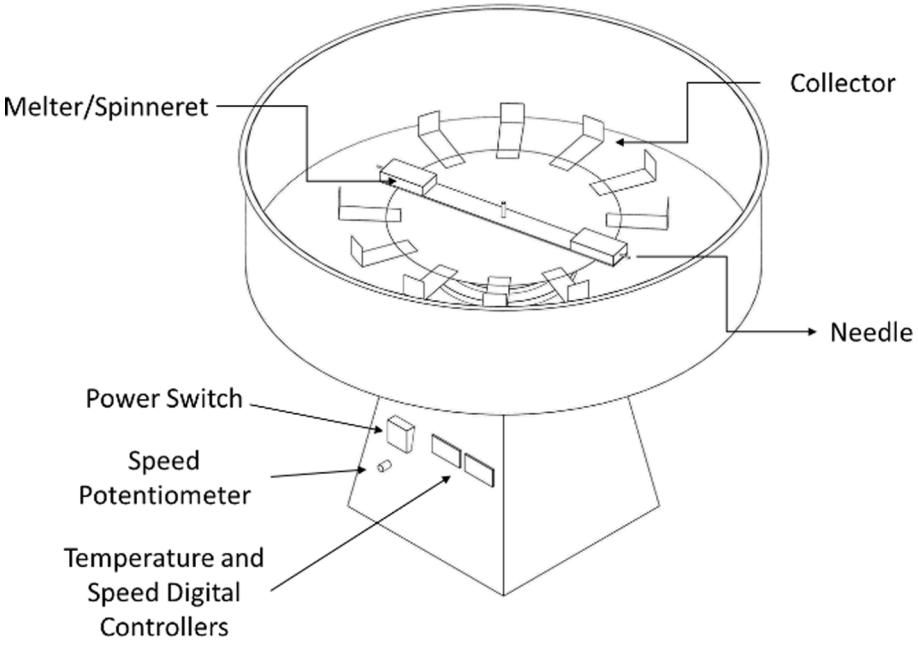

Fig. 1. Schematic of the centrifugal spinning equipment.

Table 1
Physical mixtures subjected to centrifugal spinning.

Mixture	DES	DES:PDO (%w/w)
B10	Bet-CA	10:90
B20		20:80
B50		50:50
C10	ChCl-CA	10:90
C20		20:80
C50		50:50

2.2.3. In vitro degradation test

The degradation of PDO microfibers was assessed in saline solution (NaCl 0.9 % w/v) at 37 °C ± 0.2 °C in shaking bath. Fiber disks, obtained by tabbletting 0.1 g of the yarn randomly oriented in a stainless-steel matrix (Ø= 10 mm) through a hydraulic press using 1 t force applied for 60 s, were placed a 6-well plate in 5 mL of saline solution. At fixed times, the disks were withdrawn, dried, then weighed. The weight loss was expressed as the weight loss percentage W, as follows:

$$W = (W_0 - W_t)/W_0 \times 100$$

Where W_0 was the initial weight and W_t the weight at the fixed time t.

2.2.4. Mechanical properties

The mechanical properties were assessed on fibers arranged as disks, obtained as previously described A compression test was then performed using a texture analyzer (TAXT Plus, Stable Micro Systems, Godalming, UK) equipped with a 5 kg loading cell (Sandri et al., 2020a,b). The whole disk surface (~78.54 mm^2) was compressed with a 10 mm-diameter probe (P10) and subjected to a maximum compression force of 50 N. Pre-test, test and post-test speeds were set at 0.1 mm/s, 0.1 mm/s, 5 mm/s, respectively. Analogously hydrated disks were characterized using the same approach. Dynamic compression test was performed using five compression cycles every 30 s. Stress–strain curves were recorded and the parameters were normalized for the disk depth. This allowed to evaluate the microfiber evolution upon cyclic stress application, simulating the in vivo repetitive movements. The obtained fibers were also shaped as an aligned structure using a frame consisting of iron pins placed at a fixed distance of 0.2 mm between each other. The fibers were positioned between the pins until a compact and uniform 1 cm wide structure was obtained. A tensile strength test to break point was performed. A cross-sectional area of 1 cm^2 of the aligned fibers was placed among two jaws and subjected to a total elongation of 70 mm. Pre-test, test and post-test speeds were set at 0.5 mm/s, 0.5 mm/s, 5 mm/s, respectively. A trigger force of 0.01 mN was applied. The aligned fibers were further immersed in distilled water, at room temperature, for a total time of 6 min to perform the same test in hydrated conditions. Stress–strain curves were recorded for both dry and hydrated state. A low cycle fatigue assay was then performed at the dry state to assess the material fatigue. Strain controlled cyclic tension tests were performed on all samples at dry state using the texture analyzer in the tensile mode. No significant preload (0.01 mN) and an initial strain with a magnitude of 3 % were applied. During the experiments, the strain oscillated at a frequency of 1.4 Hz with a peak-to-peak amplitude of 3 % and 10 loading cycles were performed. Then the test was conducted at the same frequency by setting 6 %, 12 %, 18 %, 24 % and 42 % of elongation. The maximum tensile strength was recorded.

2.2.5. Preclinical characterizations

2.2.5.1. Cytocompatibility, adhesion and proliferation towards normal human dermal fibroblasts (NHDFs). Normal human dermal fibroblast cells (NHDFs from juvenile foreskin, PromoCell, WVR, Italy) were grown in DMEM medium (Sigma-Aldrich, Italy) supplemented with 200 IU/mL penicillin/0.2 mg/mL (Sigma-Aldrich, Italy) and with 10 % v/v foetal bovine serum (FBS, Euroclone, Italy). Briefly, $3.5*10^4$ cells were seeded in a 96-well plate and, when the cultures reached confluency, the DES components were added, and cells were re-incubated for 3 days (Faccendini et al., 2020).

Disks, based on Bet/CA or CHCl/CA PDO microfibers, B20 and C20, respectively, were obtained by compressing 6 mg yarn randomly oriented at 2 t for 10 s with a 0.36 cm^2 surface area exposed. The disks were placed in a 96-well plate, $3.5*10^4$ cells (NHDF) were seeded onto their surface and kept in culture for 3 up to 10 days. DES components at the same theoretical amount present in 1.5, 3 and 6 mg of microfibers were also evaluated and cells grown in standard conditions have been considered as control (growth medium, GM).

Cell viability was assessed using AlamarBlue® test. AlamarBlue® test is based on resazurin that is converted by living cells in the fluorescent compound resofurin. The conversion of resazurin in resofurin

(fluorescent molecules) is directly related to cell viability. Briefly, 100 µl 10 % (v/v) AlamaBlue® in DMEM were added to each well. After 3 h, fluorescence was measured (λ_{ex} 530 nm and λ_{em} 560 nm) (FLUOstar Omega multi-mode microplate reader, BMG Labtech, Euroclone SPA, Milan, Italy). Cell viability was expressed as fluorescence intensity of each sample and compared to cells grown in standard condition (GM) (Faccendini et al., 2021): this allowed to evaluate the evolution of cell viability over time.

Confocal microscopy (CLSM) analysis allowed to visualize the NHDF adhesion and morphology onto the microfiber disks previously tested by AlamarBlue®. At 3rd and 7th days of culture, cells were fixed for 1 h at room temperature by using 3 % v/v of glutaraldehyde and then washed twice with PBS for 5 min. Substrates were permeabilized with 0.1 % w/w tryton solution for 5 min, washed twice and treated with 50 µl of FITC-phalloidin (25 µg/ml), avoiding light exposure (Sigma Aldrich, Milan, Italy). After 40 min, cells were washed twice in PBS and then the fibrous matrix marked with 100 µl of 0.5 µg/ml Hoechst 33,258 solution diluted in PBS for 10 min (Sigma Aldrich, Milan, Italy). Finally, cell nuclei were stained with 100 µl of propidium iodide (PI) (Sigma Aldrich, Milan, Italy) at 25 µg/ml for 2 min washed twice for 5 min. Then, the samples were placed on microscope slide and analyzed by using a CLSM, Leica TCS SP8 STED 3X (Leica Microsystems, Milan, Italy) at $\lambda_{ex} = 346$ nm and $\lambda_{em} = 460$ nm for Hoechst 33258, $\lambda_{ex} = 501$ nm and $\lambda_{em} = 523$ nm for phalloidin Atto 488 and $\lambda_{ex} = 488$ nm and $\lambda_{em} = 561$ nm for Propidium Iodide (PI). The acquired images were processed by means of a software (LASX, Leica Microsystem, I).

2.2.5.2. In vivo wound healing studies. All animal experiments were carried out in full compliance with the standard international ethical guidelines (European Communities Council Directive 86/609/EEC) approved by Italian Health Ministry (D.L. 116/92). The study protocol was approved by the Local Institutional Ethics Committee of the University of Pavia for the use of animals and by ISS (Istituto Superiore di Sanità). Six male rats (Wistar 200–250 g, Envigo RMS S.r.L.) were anesthetized with equitensine at 3 mL/kg (39 mM pentobarbital, 256 mM chloral hydrate, 86 mM MgSO4, 10 % v/v ethanol, and 39.6 % v/v propylene glycol) and shaved to remove all hair from their backs. The animals were kept separately in different cages (one per cage) throughout the experiment. In the supplementary information a scheme of the treatments is reported: to each rat an ID number was assigned, and all the tissue samples obtained from the experiments were coded using rat ID plus a specific code number (Table S1).

2.2.5.2.1. Evaluation of systems safety. To analyze the in vivo reactions triggered by the systems, a subcutaneous implant model was employed (Al-Maawi et al.,2018). Disks based on Bet/CA and CHCL/CA PDO fibers (2 t for 10 s) having 4 mm diameter were subcutaneously implanted by means of an 8 mm incision (one for each rat) in the rats back. The six rats were divided in two groups of three to evaluate the different systems. The incisions were then sutured using strips (Steri-Strip Suture, Italy). After the treatment (18 days), full thickness biopsies were taken in correspondence of the incisions and the histological analysis was performed. A biopsy of intact skin was also taken for comparison.

2.2.5.2.2. Evaluation of systems efficacy on excisional/burn model. Three circular full thickness burns, 4 mm in diameter, were produced on the back of the animals by contact with an aluminum rod (105 °C for 40 s). After 24 h, the formed blisters were removed using a 4 mm diameter biopsy punch to obtain a full-thickness lesions. Two full thickness lesions were treated with each scaffold and the third lesion with saline solution. Scaffolds having 4 mm diameter (as big as the lesions) were applied and wetted with 20 µl of saline solution (0.9 g/l). Lesions treated with 20 µl saline solution were the negative control. Lesions were covered with a sterile gauze and the rat back was wrapped with a surgery stretch (Safety, Italy) to protect lesions. At prefixed times after blister removal (0, 3, 7, 10, 14 and 18 days) photographs of the lesions were taken by using a digital camera (Sigma SD 14) for sizing the lesions and monitoring the healing process. The size of wounded area was determined with an image analysis software (Image J, ICY, Institute Pasteur, France). Eighteen days after the treatment, full thickness biopsies were taken in correspondence of the initial lesions and the histological analysis of the excised tissues was performed. A biopsy of intact skin was also taken for comparison.

2.2.5.2.3. Histological analysis. Tissue samples were bisected, immediately immersed in the fixative solution (10 % v/v neutral buffered formalin), embedded in paraffin, and sectioned at a thickness of 5 µm. Some sections were stained with hematoxylin and eosin (H&E), others with picrosirius red (PSR). Picrosirius red stain was applied as follows: deparaffinized sections were hydrated, faintly stained with Weigert's hematoxylin for nuclei, and stained with PSR (1 h). Then all sections were dehydrated, cleared in xylene, and mounted with DPX. Stained sections were observed with a light microscope Carl Zeiss Axiophot provided, for circular polarizing microscopy, with suitable filters in the condenser stage and in the microscope tube. Images were recorded through a microscope digital 5 megapixels CCD camera Nikon DS - Fi2.

2.2.6. Statistical analysis

Statistical analyses were performed using Astatsa statistical calculator. One-way analysis of variance (ANOVA) was followed by Scheffè for post-hoc comparisons. $p < 0.05$ was considered significant.

3. Results and discussion

3.1. Physical-chemical characterization

3.1.1. Microfiber morphology and size

The addition of DES to PDO as a physical mixture is essential for fiber formation by centrifugal spinning. As already confirmed by literature (Roda et al., 2019), the DES acts as a plasticizer and positively affects the extrusion and stretching of polymer and DES blends from the spinneret during the spinning process. Moreover, the microfiber % yield is higher when PDO is 80 % in the blends (Table 2).

Independently of the PDO/DES ratio and the DES type, microfiber diameters are comparable and are conceivably mainly influenced from the spinneret orifice dimension that is the main responsible of the system morphology as shown in Fig. 2.

Given the % higher yield, B20 and C20 are selected for further characterizations. Microfiber hydration (7 days in pH 7.4 PBS at 37 °C) affects the surface morphology and microfractures are present on the fiber surface, markedly evident in B20 (Fig. 3, red arrows). Moreover, the hydration causes the decrease of fiber diameter: in particular, for B20, the diameter is 15.78 ± 8.26 with a 7.3 % decrease, although it is not significant, while for C20 it is 13.40 ± 5.78 with a 22.1 % significant decrease. This is conceivably related to the hydrolytic degradation of esters bonds, that occurs at 37 °C in PBS. It is reported in literature that

Table 2
Fiber composition, yield (%) and fiber diameter (mean values ± s.d.; n=3). Statistical analysis: 1-way ANOVA, Test Sheffé: C10 vs C20 p = 0.002; C10 vs C50 p = 0.001; C10 vs C80 p = 0.001. C20 vs C50.

Mixture	DES	DES:PDO ratio (%w/w)	% Yield	Mean fiber diameter (µm)
PDO	/	100 % PDO	/	/
B10	Bet/CA	10:90	9.5 %	19.00 ± 8.78
B20		20:80	20.5 %	17.02 ± 11.64
B50		50:50	22.8 %	16.18 ± 8.74
B80		80:20	5.3 %	18.36 ± 7.33
C10	ChCl/	10:90	6.0 %	22.58 ± 9.00
C20	CA	20:80	24.0 %	17.21 ± 9.30
C50		50:50	7.5 %	14.66 ± 6.67
C80		80:20	5.5 %	14.97 ± 6.82

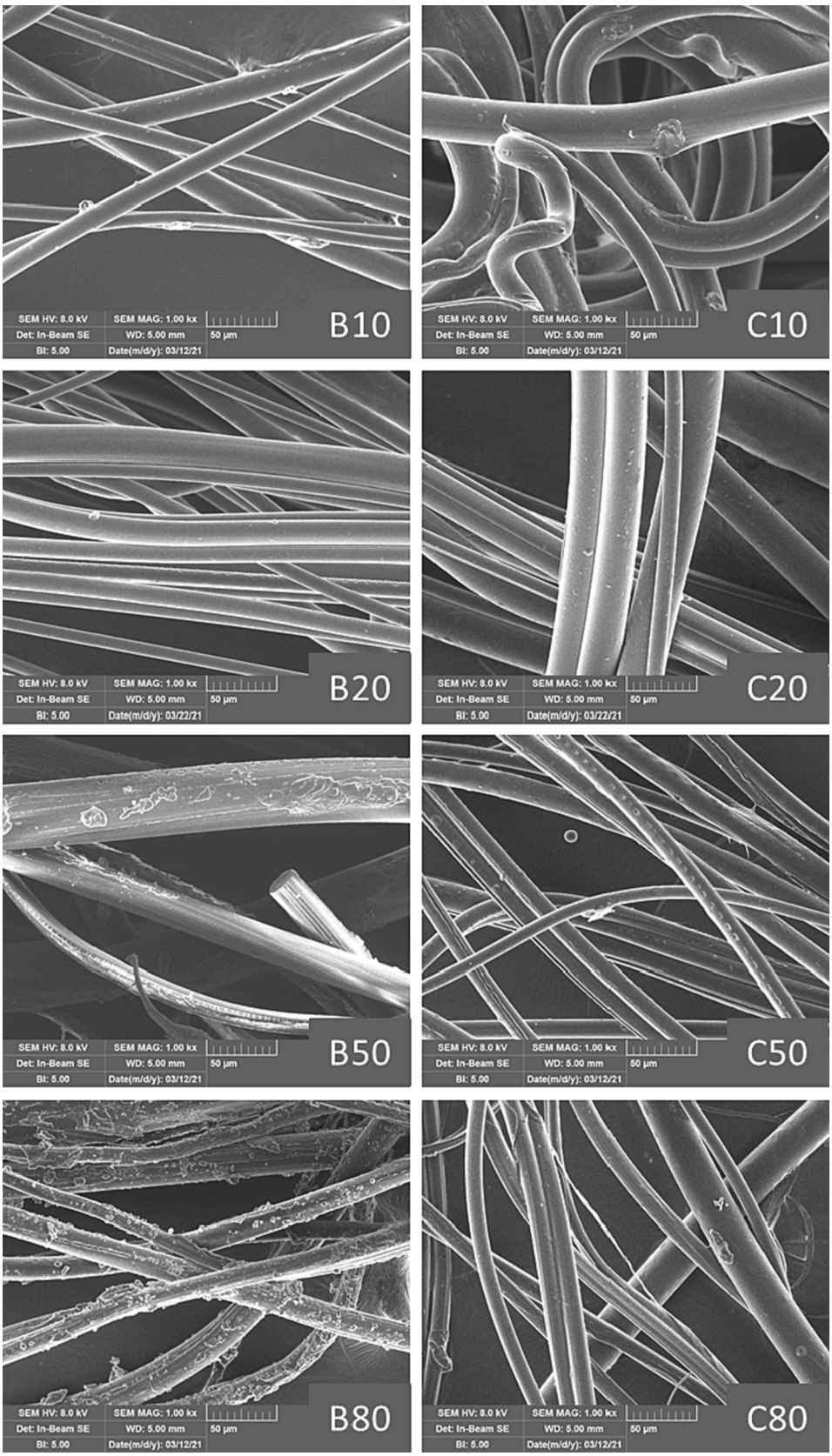

Fig. 2. Micrographs SEM of PDO fibers prepared using Bet/CA (B) or CHCl/CA (C) DES at different weight ratios. Fibers are characterized by smooth and continuous fibers of approximately 1 m length (scale bar 50 μm).

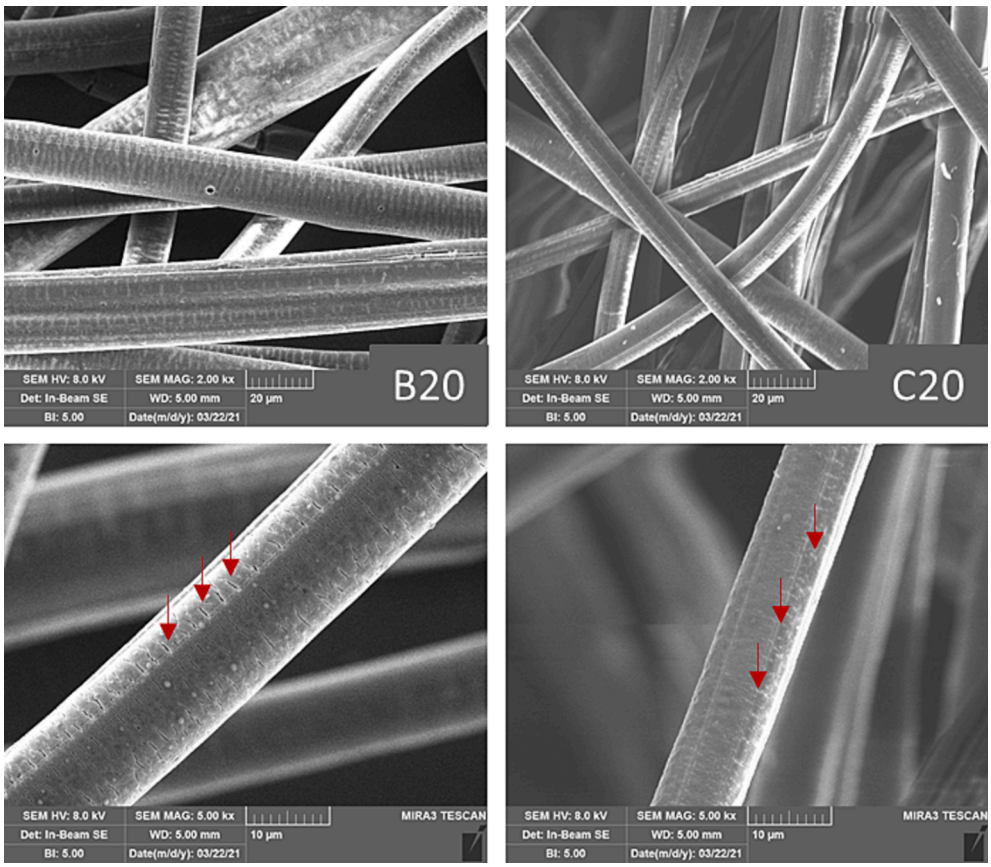

Fig. 3. SEM micrographs of B20 and C20 after hydration in PBS at 37 °C for 7 days (up panels 2 kx magnification; down panel 5 kx magnifications) (scale bars 20 μm up panel and 10 μm down panel) (red arrows: microfractures).

the hydrolytic degradation of PDO, occurs in two steps: at first the chain break happens in amorphous regions where water enters into inter-microfibrillar space faster than into the crystalline regions. Subsequently hydrolytic degradation advances in crystalline regions. This means that the lowest crystallinity the highest degradation rate (Kang and Song, 2022). The presence of DES that act as plasticizer increases the hydrolytic degradation since they decrease the crystallinity of the polymers.

The degradation of the microfibers in aqueous environment was also quantified and is not related to DES type but it is conceivably led by PDO solid state (Fig. 4). Despite this, microfibers containing betaine seems slightly resistant to degradation and the weight loss is close to 62 % for B20 while is almost 70 % for C20, in agreement with the SEM analysis. Moreover, the B20 specific surface area (SSA) is higher than that of C20

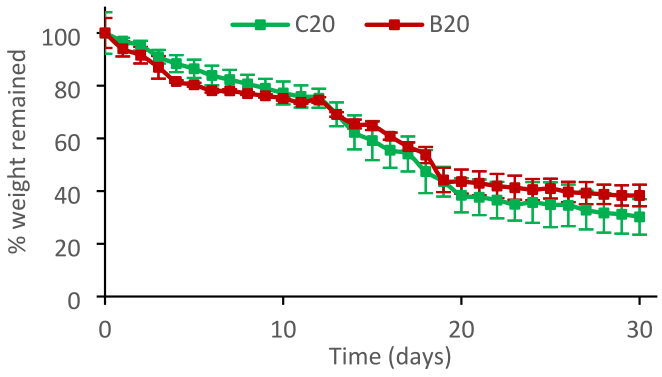

Fig. 4. % weight loss of C20 and B20 microfibers after saline solution treatment at 37 °C for 30 days. (mean values, ±s.d.; n = 3).

and they are 21.16 μm^{-1} (±0.10) for B20 and 16.82 μm^{-1} (±0.81) for C20 and both results suggest that the microfibers possess a high surface (Chen et al., 2009).

3.1.2. *Thermal analysis*

To better understand the solid state change caused by the spinning process and its influence on the functional properties of the microfibers, thermal analysis was performed. Fig. 5 reports the TGA profiles, and in particular Fig. 5a shows the behavior of the pristine components, Fig. 5b reports the thermal behavior of the microfibers while the Fig. 5c reports the thermal behavior of the microfibers subjected to thermal treatment in the conditions of the manufacturing process (isothermal profile at 140 °C for 10 min). The weight losses are evident for the pristine components (Fig. 5a) at temperatures higher than 140 °C (vertical black line in each graph). This is also confirmed in both the microfibers type and independently of the isothermal treatment at 140 °C (Fig. 5b and c). Moreover, at 140 °C the weight losses for the formulations are negligible in all cases and lower than 1 % w/w.

DSC profiles confirm the system stability at the spinning temperature (Fig. 6). In particular, the pristine components, except citric acid, are characterized by melting. PDO melts at about 112 °C and the sharp peak suggests a high polymer crystallinity, while both ChCl and Bet melt at about 309 °C (Fig. 6a). In the microfibers the melting peaks are less sharp and occur at lower temperature (106 °C) for both the formulations B20 and C20. This is conceivably related to the PDO melting that is probably lowered due to the plasticizing effect of both the DES, Bet/CA or ChCl/CA. The plasticizing function is attributable to the liquid state of DES at room temperature that are completely amorphous (Hansen et al., 2020a,b; Shafie et al., 2019; Aroso et al., 2017) due to the complexation of the quaternary ammonium salt (either choline or betaine) and the hydrogen bond donor (citric acid monohydrate) (Mori and Usuki, 2022;

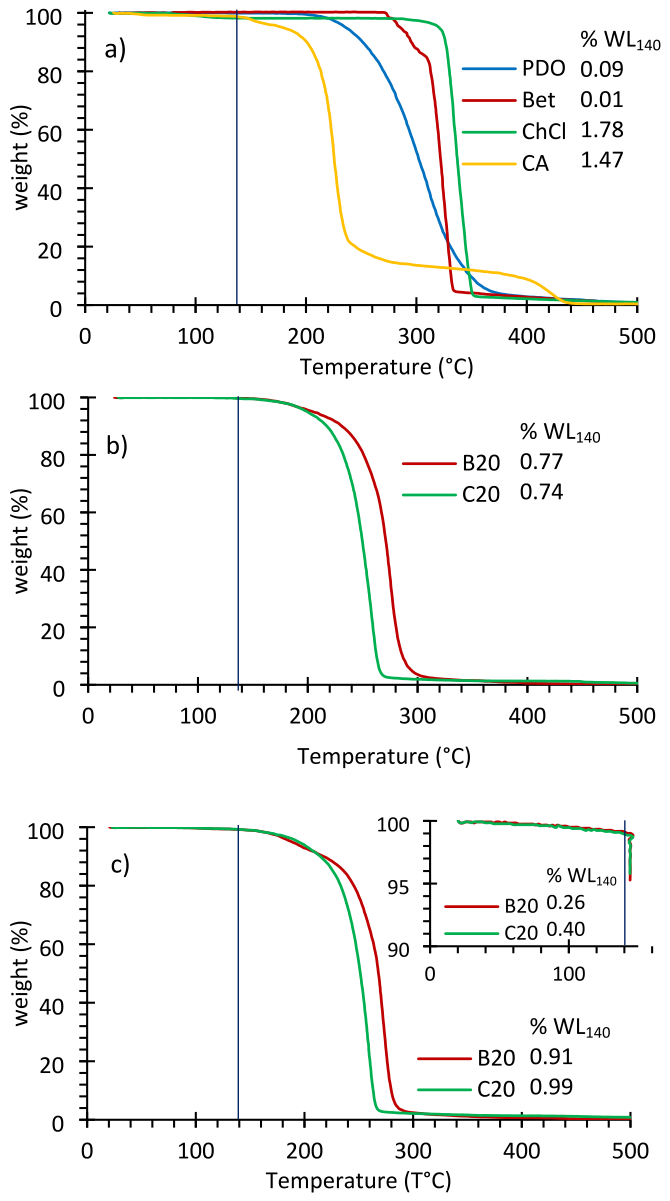

Fig. 5. TGA: a) raw materials; b) B20 and C20 (10 °C/min); c) B20 and C20 (10 °C/min after isotherm 145 °C for 10 min (in the inset) (black line 140 °C: spinning temperature). In the insets, the % weight loss at 140 °C (% WL_{140}) is reported.

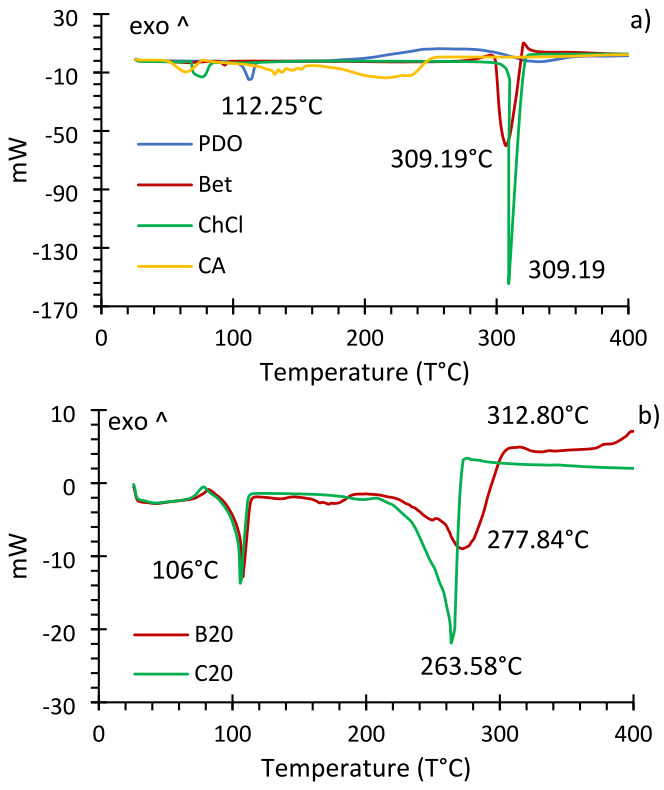

Fig. 6. DSC spectra: a) pristine materials; b) B20 and C20 (10 °C/min).

Hansen et al., 2020a,b; Aroso et al., 2017). At a temperature higher than 140 °C, and precisely at 277, and 263 °C for B20 and C20 microfibers, respectively, other endothermic peaks are present. These are in correspondence to the marked weight losses (in TGA Fig. 5) and are conceivably due to the microfiber degradation. These findings suggest that PDO is characterized by less thermal stability at temperature higher than 200 °C in the microfibers since the complete thermal degradation is steeper and at lower temperature, compared to the pristine polymer in TGA (Fig. 5), and causes a widen endothermic peak at lower temperature, in DSC analysis (Fig. 6), both behaviors conceivably related to the poor polymer crystallinity due to the DES. These results strengthen the hydrolytic degradation visible in the SEM images upon microfiber hydration (Fig. 3) and confirmed by degradation study (Fig. 4).

3.1.3. *Chemical structure analysis*

The microfiber chemical structure was investigated using NMR spectroscopy and the NMR spectra of B20 and C20 fibers are reported in Fig. 7 in the upper and bottom panels, respectively. All the chemical shift values range from 2.0 to 4.5 ppm. Moreover, the signals related to the pristine components are all present in the final microfiber structure. In particular, in the spectrum of B20, the doublet of doublet peak (δH 2.57 ppm) corresponding to citric acid is visible, moreover, the singlet (δH 3.3 ppm) related to betaine and the triplet (δH 3.55 ppm), singlet (δH 3.90 ppm) and triplet (δH 4.10 ppm) of PDO structure are also recognizable. The signals of citric acid, choline chloride, and PDO are also evident in C20. The singlet (δH 2.92 ppm), corresponding to choline chloride, and the PDO characteristic peaks are evident and confirm the identity of the spun matrix. In both cases, the process does not change the structure of the components suggesting that no degradation or grafting occur in the manufacturing conditions.

3.2. *Mechanical properties*

Since the healing process could be easily altered and impaired by external mechanical forces (Fang et al., 2020), a scaffold suitable to sustain wound healing should maintain its 3D structure and recover it upon mechanical stress, with a minimal deformation to maintain 3D architecture. Given this, microfibers were subjected to cyclic mechanical stresses to characterize their mechanical properties. In this perspective, microfibers have been tested in random – disks - and in aligned – rope – 3D organization. Fig. 8 reports the compression degree and the tensile strength evaluated in both the 3D organization, in dry and hydrated conditions.

In random 3D organization, C20 fibers are characterized by compressibility higher than B20 at dry and hydrated conditions and the hydration does not affect this. However, both B20 and C20 random microfibers in disks, show a little compression deformation equal to 15 and 25 %, respectively (Fig. 8a), suggesting that the structures are resistant to compression stress giving a prediction of the scaffold fate upon implant. Moreover, the disks are characterized by high resistance to repeated compression (Fig. 8b) and no change in deformation is evident. Furthermore, the aligned fibers (rope) better show the typical

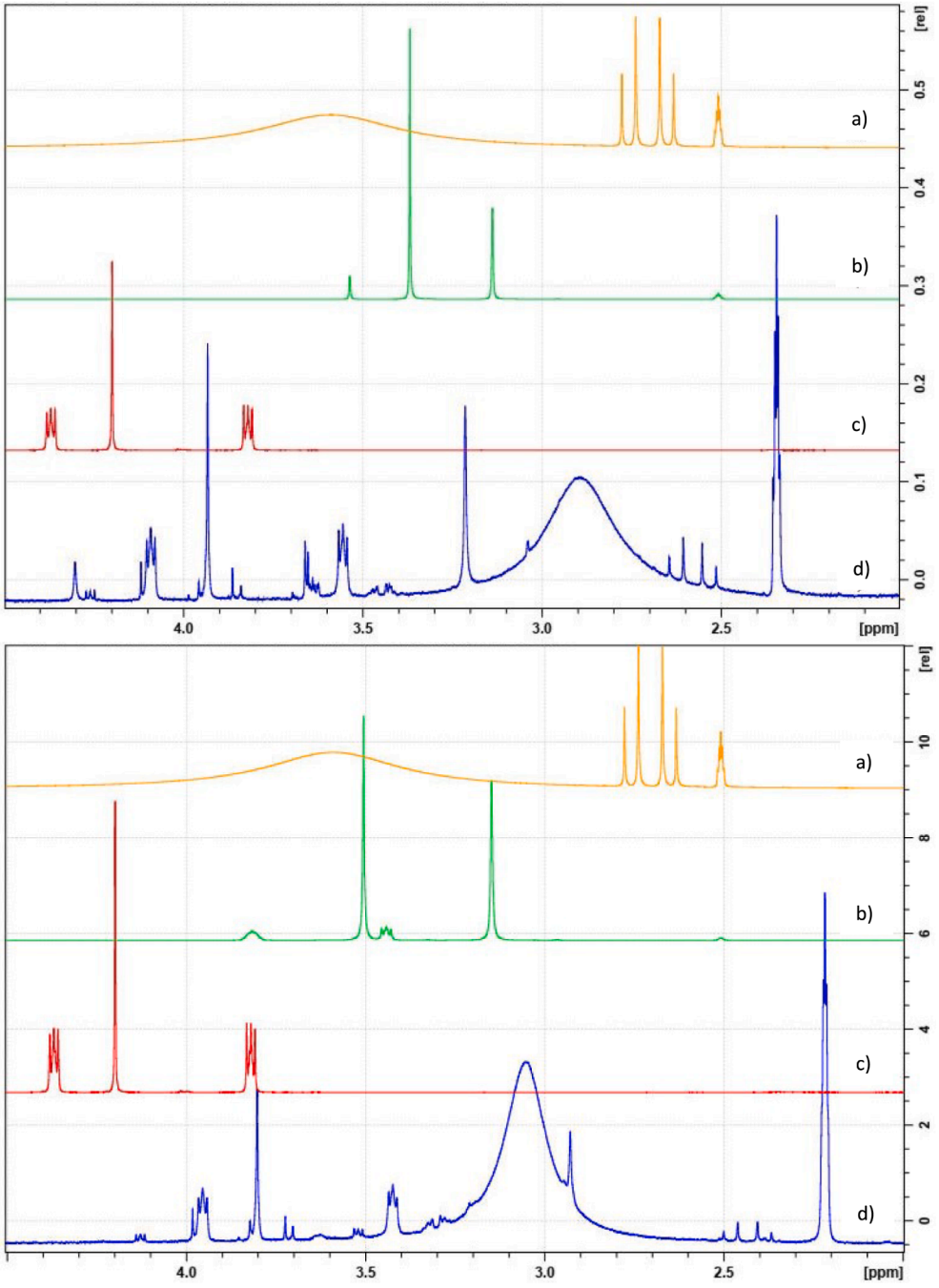

Fig. 7. NMR spectra up panel: a) CA in DMSO-d_6; b) Bet in DMSO-d_6; c) PDO in $CDCl_3$; d) B20 fibers in $CDCl_3$ + DMSO-d_6. low panel - a) CA in DMSO; b) CHCl in DMSO c) PDO in $CDCl_3$; d) C20 fibers in $CDCl_3$ + DMSO.

trend of a quasi-brittle materials, as hard and strong materials and, also in this fiber organization, the hydration does not significantly modify the mechanical properties. The strain intensively modifies the tensile strength. The increase of elongation is related directly to the recorded strength values of up to 42 % of B20 microfiber extension. On the contrary, C20 proportionally shows an increase in strength up to 18 % strain as a yield point and a lowering in stress values for higher elongations. This is conceivably related to the relaxation of the structure and to a softening since this possesses the behavior of rigid plastic materials.

To better characterize the stiffness/elastic behavior of the fibers, the Young's modulus has been calculated in the linear region of 8 % strain/stress curve for the compression test and the linear region of 10 % strain/stress curve for the tensile strength test (Table 3). The elasticity is similar independently of the fiber type and the hydration when the 3D organization is random. On the contrary, the alignment puts in evidence that the C20 fibers are highly elastic compared to B20, and this is confirmed by the degradation (Fig. 4, faster than that of B20) and the thermal (Fig. 6, lower melting) behaviors. In addition, in both compositions, the hydration causes a loss in elasticity. It is probably related to the softness of the single fiber that prevails in the resistance of the 3D organization.

3.3. Preclinical characterizations

3.3.1. Cytocompatibility, adhesion and proliferation towards normal human dermal fibroblasts (NHDFs)

The assessment of in vitro preclinical effectiveness to stimulate cell

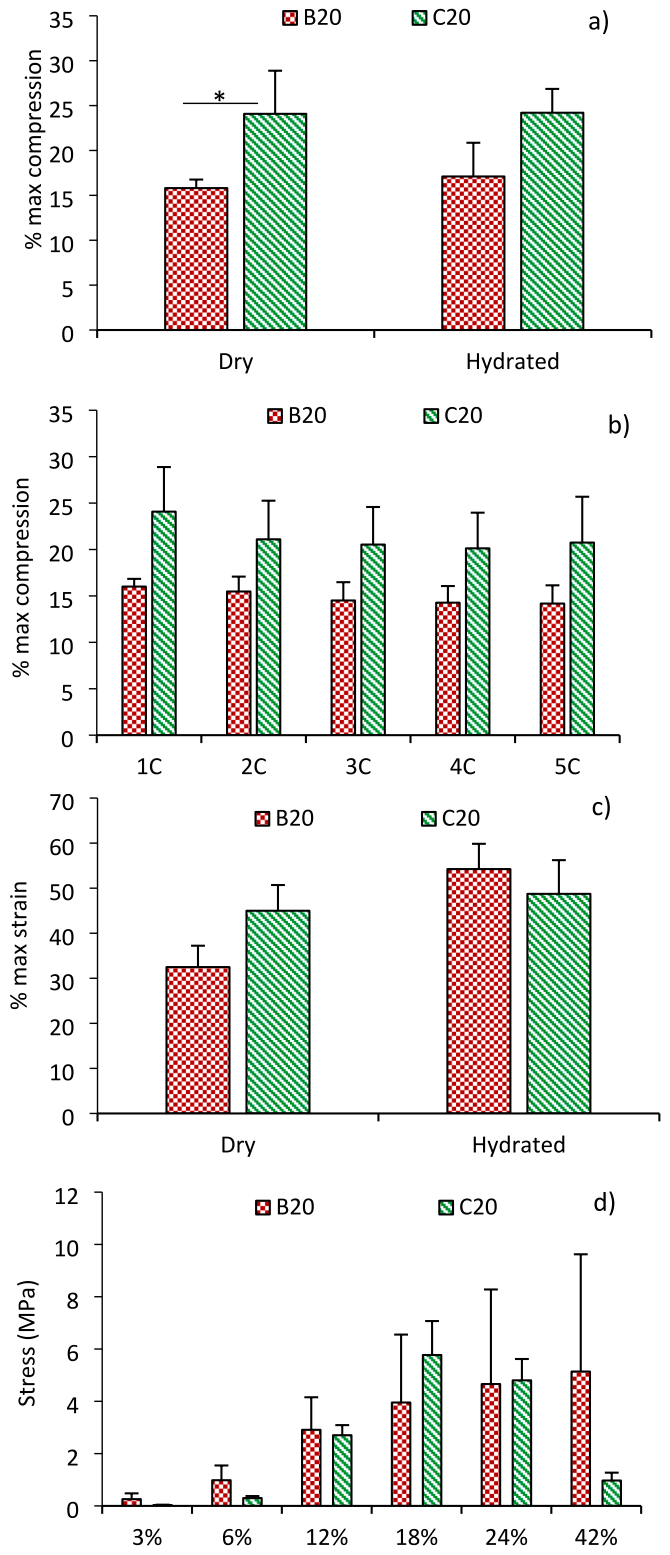

Fig. 8. Mechanical properties of the fibers in disks (random): a) maximum compression (%) before (dry) and after hydration (hydrated); b) repeated compression of the disks in dry state (C = cycle). Mechanical properties of the fibers in rope (aligned): c) maximum strain (%) at break point before (dry) and after hydration (hydrated); d) maximum stress values (MPa) after tensile strength test at different elongation (%) (mean values ± s.d., n = 5). Statistical analysis: 1-way ANOVA, post-hoc Scheffé test: * $p < 0.05$.

Table 3
Young Modulus (MPa) calculated for dry and hydrated fibers, as disks (random) and rope (aligned) (mean values ± s.d., n = 5). Statistical analysis: 1-way ANOVA; Test Scheffé $p < 0.05$.

Fiber type	Young Modulus (MPa)	
	Disks	Aligned
B20-Dry	1.16 ± 0.03	3.08 ± 2.32
B20-Hyd	1.15 ± 0.03	2.02 ± 0.82
C20-Dry	1.09 ± 0.04	3.70 ± 0.71
C20-Hyd	1.05 ± 0.05	3.30 ± 0.68

homing by enhancing fibroblasts migration, adhesion and proliferation, was assessed using normal human dermal fibroblasts, seeded onto 3D PDO scaffolds.

Fig. 9 reports the cytocompatibility of fibroblasts seeded in presence of pristine components (Fig. 9a) and onto the microfiber disks (Fig. 9b) and grown for 3 days. All DES components are characterized by good cytocompatibility, up to 1600 μg/ml concentration, except for citric acid which causes a significant decrease in the pH medium justifying its negative effect. Alongside, the 3D scaffolds are characterized by good biocompatibility towards fibroblasts and the microfibers are able to sustain the cell growth up to 10 days. In particular fibroblasts show a rapid proliferation up to the 3rd day, while the growth reaches a plateau in the subsequent days up to the 10th day, suggesting that the cells reach confluency. On the contrary, the cell substrate grown in the standard growth condition (GM) is characterized by a significantly higher cell growth up to the 6th day and a subsequent significant decrease of cell viability suggesting that fibroblasts growth is limited for prolonged times. Neither the DES nor the manufacturing process impair the

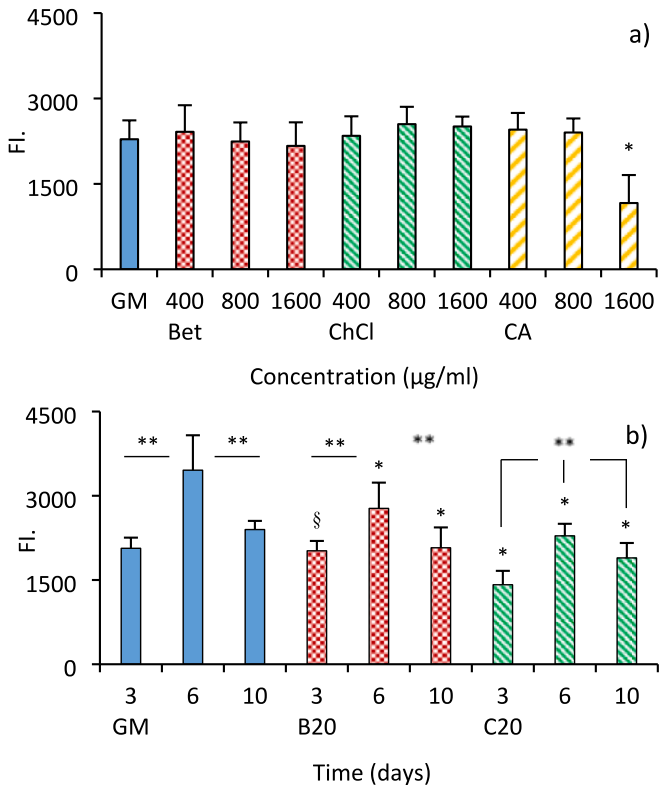

Fig. 9. Fibroblasts (NHDF) viability (FI, fluorescence intensity): a) 3-days contact with DES components; b) 3-, 6- and 10-days contact of B20 and C20 disks (mean values ± s.d.; n = 8). Statistical analysis: 1-way ANOVA post hoc Scheffè test $p < 0.05$: a) * GM vs 1600 μg/ml CA; b) * GM vs B20; GM vs C20 fibers; § B20 vs C20; ** GM 3d vs GM 6d and GM 6d vs GM 10d; B20 3d vs B20 6d and B20 6d vs B20 10d; C20 3d vs C20 6d, C20 3d vs C20 10d and C20 6d vs C20 10d.

biocompatibility of PDO. These results are in line with previous studies that prove PDO-based scaffolds as excellent support for mesenchymal stem cells (MSC) and in particular for human adipose stem cells (hASC) inducing differentiation into adipogenic, osteogenic, and chondrogenic cells in vitro (Saska et al., 2021; Goonoo et al., 2019; Rowland et al., 2016). Furthermore PDO-based scaffolds also prove to sustain fibroblasts proliferation and modulate extracellular matrix deposition (Yue et al. 2019; Chummun et al., 2018; Ramphul et al., 2017).

The confocal images (Fig. 10) support the cytocompatibility findings. The cell nuclei (in red) appear well preserved in all cases and the cell cytoskeletons (in green) are fusiform and stretched along the microfibers forming in some cases bridges between the fibers (in blue). The fibroblasts are able to spread onto the structure in depth and to establish multiple contacts with one fiber and the surrounding ones. The microstructure is confirmed as essential to promote cell adhesion and proliferation and the high SSA seems favorable to promote cell adhesion (Wang et al., 2022; Xu et al., 2022; Huang et al., 2022; Jia et al., 2021).

3.3.2. *In vivo wound healing studies: Safety and efficacy*

The safety and efficacy of the microfibers was assessed in vivo in a rat burn/excisional wound model. The histological evaluation was performed 18 days post-implant.

Fig. 11 reports the representative images of the tissues in correspondence to the subcutaneous implants of B20 and C20 fibers in disks (random 3D organization), aiming at studying the scaffold safety. In Fig. S1 (see supplementary information) the histological analysis of the tissues in correspondence to all the subcutaneous implants are reported.

H&E images (Fig. 11 a, b) show that numerous microfibers are visible in the dermis, indicating a not complete degradation upon implant (green arrows), in agreement with the degradation study. Despite this, a minimum inflammatory pattern is present and PSR and PSR under the polarized light highlight collagen bundles (Fig. 11 c-f). This is confirmed by other studies that describe an inflammatory response following PDO implant milder than that of other polyesters-based implants (Martins et al., 2020; Wada et al., 2001).

PDO is reported as able to trigger neocollagenesis upon implant and the biostimulation starts with the production of type I collagen by the dermal tissue, then gradually converted to type III collagen. Moreover PDO, characterized by a quite slow degradation rate, is confirmed as able to act as homing agent for fibroblasts and endothelial cells (Ha et al, 2022).

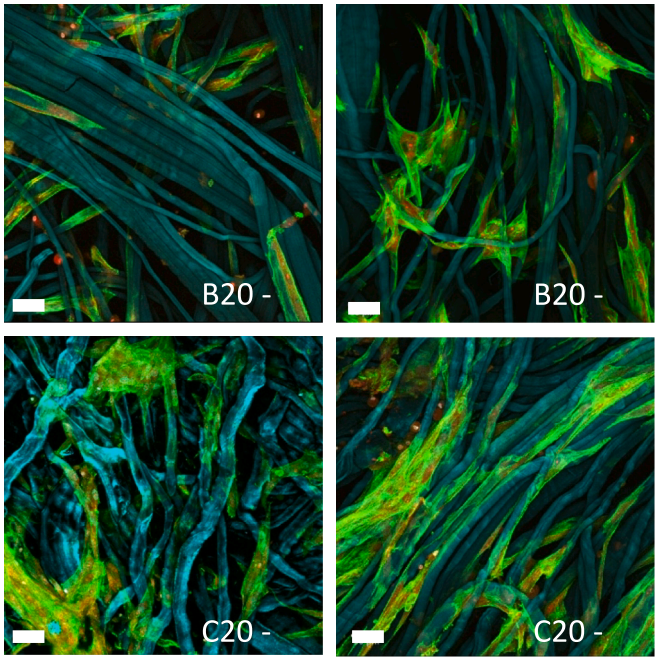

Fig. 10. CLSM images of NHDF seeded onto B20 and C20 disks after 3 and 7 days (scale bar 50 μm) (nuclei in red; cytoskeleton in green), fibers in light blue). (For interpretation of the references to colour in this figure legend, the reader is referred to the web version of this article.)

The scaffold efficacy was investigated in vivo by implanting the scaffolds (microfiber disks - random 3D organization) in cutaneous full thickness burn/excisional lesions. Fig. 12 reports the profiles of wounded area reduction vs time of the lesions treated using B20 and C20 implant and the control, while Fig. 13 reports the representative images of the histology performed in correspondence of the lesions, moreover, Figs. S2 and S3 (see supplementary information) reports the histological analysis of the tissues in correspondence to all the scaffold implants in the full thickness lesions. All the lesions decrease their dimension with a similar behavior (Fig. 12) independently of the type of treatment (implant of the microfibrous scaffolds or the lesion treated with saline solution, as negative control). However, the histology of the tissues in the treatment area after 18 days from the implants (Fig. 13) show different grade of evolution. In particular, wound closure with completely regenerated epithelium is assessable in all the area treated with the fibers. B20 and C20 allow to complete restore the epidermis integrity in cell multiple layers with a stratum corneum reformed. Collagen is loosely arranged in the underlying dermis in an orderly pattern. Moreover, zones of normal collagen tissue are also present. Overall, collagen is remodeled in an appropriate orientation to withstand the tensile stresses placed on the area of repair, suggesting a maturation and advanced remodeling phase (Singer and Clark, 1999). Both microfiber disks show effectiveness in skin healing when compared to the negative control (wound treated with physiological solution), and this is conceivably due to the stimulation of re-epithelization and the accelerated collagen deposition. It is not possible to individuate microfibers in the wounded area restored and this could be due to the healing process that starts from the wound bed and could remove microfiber residues during cell proliferation.

On the contrary, in the negative control, wound area treated with saline solution, shows a partial re-epithelialization and a large amount of thin newly formed collagen fibers. Furthermore, PSR staining shows a continuous collagen layer, rich in orange-to-red fibers in all the samples, confirmed by the images under a polarized microscope. The results are in agreement with literature since PDO has been characterized as able to stimulate in vivo collagen synthesis without generating fibrosis (Kwon et al. 2019; Zhou et al.2019) and PDO scaffolds prove to be histoconductive and to induce neocollagenesis (Saska et al., 2021, Kwon et al. 2019; Zhou et al. 2019). The degradation time, the mechanical properties and the neocollagen synthesis contribute to enhance wound reparation (Degreef, 1998; Dhivya et al., 2015).

In addition DES made of betaine and choline and citric acid, together with the pH decrease due to PDO degradation, could avoid microbial infections by controlling the scaffold colonization. This finding has been suggested by Zhang (Zhang et al., 2022) and it is conceivable related to the high density of –OH and –COOH groups.

4. Conclusions

PDO microfibers have been successfully manufactured using centrifugal spinning, using a green, sustainable manufacturing process with lower energy consumption. Moreover a solvent-free process has been developed using deep eutectic solvents, DES, as plasticizers and betaine/citric acid or choline/citric acid (both at 1:1 wt ratios) have been considered. DES:PDO 20:80 ratio allows to obtain suitable process yield and, independently of the DES, the microfibers have diameters ranging from 10 to 20 mm with a smooth surface. The solid state characterization confirms the microfiber stability to the manufacturing process. The analysis of the mechanical properties suggests that the microfibers are resistant to compression (in disk, random 3D organization) and to tensile strength (in rope, aligned 3D organization) with high elasticity and

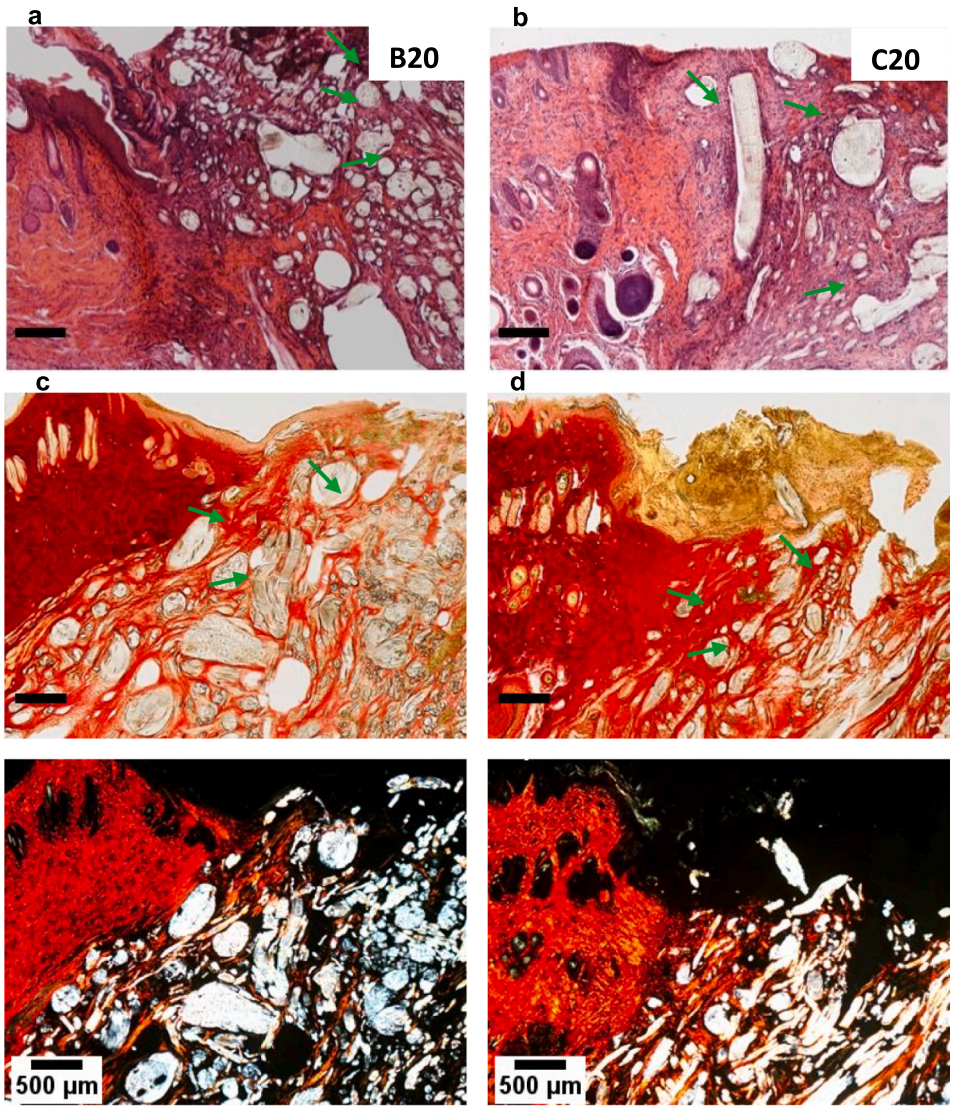

Fig. 11. Histology of the subcutaneous implant: a-b) H&E; c-d) picrosirius red, normal light; e-f) picrosirius red polarized light (scale bars: 500 µm). Green arrows indicate the microfibers implanted. (For interpretation of the references to colour in this figure legend, the reader is referred to the web version of this article.)

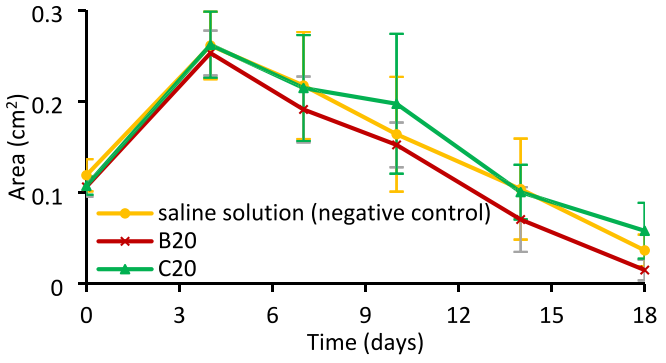

Fig. 12. Wound area (cm^2) vs time of the lesions treated with B20 and C20, in comparison to saline solution (mean values ± s.d.; n = 6).

minimal deformation, both required for in vivo implant performance. The hydration minimally affects the fiber morphology and the degradation is as slow as to sustain fibroblasts homing and proliferation. Moreover, the microfibers are cytocompatible towards human fibroblasts in vitro and prove to be characterized by excellent safety and efficacy profiles in an vivo burn/excisional murine model.

CRediT authorship contribution statement

Dalila Miele: Validation, Formal analysis, Investigation, Data curation, Writing – original draft, Writing – review & editing, Visualization. **Cristian Nomicisio:** Validation, Formal analysis, Investigation, Data curation. **Giorgio Musitelli:** Methodology. **Cinzia Boselli:** Validation, Formal analysis, Investigation. **Antonia Icaro Cornaglia:** Validation, Formal analysis, Investigation, Resources. **Rita Sànchez-Espejo:** Investigation, Data curation. **Barbara Vigani:** Investigation. **Cesar Viseras:** Resources, Funding acquisition. **Silvia Rossi:** Resources, Funding acquisition. **Giuseppina Sandri:** Conceptualization, Resources, Writing – original draft, Writing – review & editing, Visualization, Supervision, Project administration, Funding acquisition.

Declaration of Competing Interest

The authors declare that they have no known competing financial interests or personal relationships that could have appeared to influence the work reported in this paper.

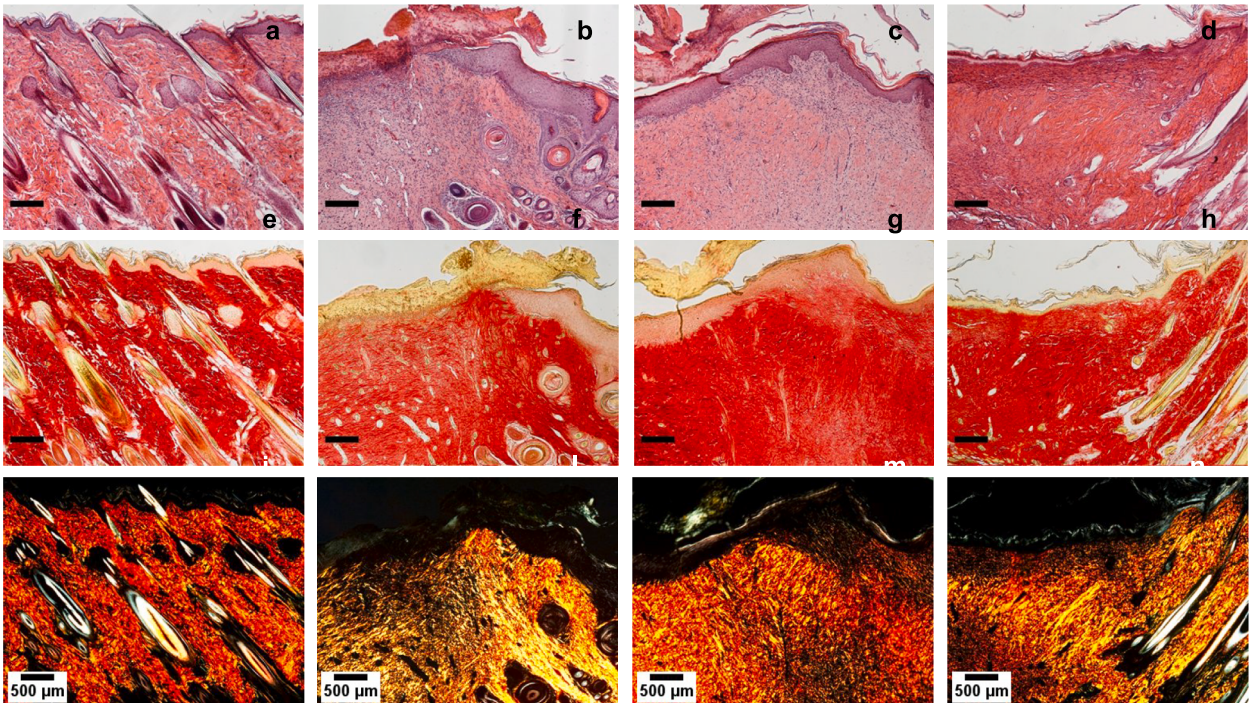

Fig. 13. Histology: a-d) H&E staining; e-h) picrosirius red normal light; i-n) picrosirius red polarized light; a,e,i) intact skin, control; b, f, l) B20; c, g, m) C20; d, h, n) untreated lesion (saline solution), negative control. column B) negative control (scale bars: 500 μm). (For interpretation of the references to colour in this figure legend, the reader is referred to the web version of this article.)

Data availability

Data will be made available on request.

Acknowledgements

DM wishes to thank FRG, University of Pavia, to grant her post-Doc position. CN wishes to thank Programma Operativo Nazionale Ricerca e Innovazione 2014-2020 (PON R&I 2014-2020) for his PhD position.

The authors wish to thank Giampiero Piva for the technical support to the development of the centrifugal spinning apparatus.

Appendix A. Supplementary data

Supplementary data to this article can be found online at https://doi.org/10.1016/j.ijpharm.2023.122669.

References

Al-Maawi, S., Vorakulpipat, C., Orlowska, A., Zrnc, T.A., Sader, R.A., Kirkpatrick, C.J., Ghanaati, S., 2018. In vivo implantation of a bovine-derived collagen membrane leads to changes in the physiological cellular pattern of wound healing by the induction of multinucleated giant cells: an adverse reaction? Front. Bioeng. Biotechnol. 104 https://doi.org/10.3389/fbioe.2018.00104.

Aroso, I.M., Paiva, A., Reis, R.L., Duarte, A.R.C., 2017. Natural deep eutectic solvents from choline chloride and betaine–Physicochemical properties. J. Mol. Liq. 241, 654–661. https://doi.org/10.1016/j.molliq.2017.06.051.

Boland, E.D., Coleman, B.D., Barnes, C.P., Simpson, D.G., Wnek, G.E., Bowlin, G.L. 2005. Electrospinning polydioxanone for biomedical applications. Acta Biomater. 1(1), 115-23. 110.1016/j.actbio.2004.09.003. PMID: 16701785.

Chaim, I.A., Sabino, M.A., Mendt, M., Muller, A.J., Ajami, D., 2012. Evaluation of the potential of novel PCL/PPDX biodegradable scaffolds as support materials for cartilage tissue engineering. J Tissue Eng. Regen. Med. 6, 272–279. https://doi.org/10.1002/term.430.

Chen, M., Patra, P.K., Lovett, M.L., Kaplan, D.L., Bhowmick, S., 2009. Role of electrospun fibre diameter and corresponding specific surface area (SSA) on cell attachment. JTERM 3 (4), 269–279. https://doi.org/10.1002/term.163.

Chouhan, D., Dey, N., Bhardwaj, N., Mandal, B.B., 2019. Emerging and innovative approaches for wound healing and skin regeneration: Current status and advances. Biomaterials 216, 119267. https://doi.org/10.1016/j.biomaterials.2019.119267.

Chummun, I., Bhaw-Luximon, A., Jhurry, D., 2018. Modulating matrix-multicellular response using polysucrose-blended with poly-L-lactide or polydioxanone in electrospun scaffolds for skin tissue regeneration. J. Biomed. Mater. Res. A 106 (12), 3275–3291. https://doi.org/10.1002/jbm.a.36527.

Dai, Y., van Spronsen, J., Witkamp, G.-J., Verpoorte, R., Choi, Y.H., 2013. Natural deep eutectic solvents as new potential media for green technology. Anal. Chim. Acta. 766, 61–68.

Degreef, H.J., 1998. How to heal a wound fast. Dermatol. Clin. 16 (2), 365–375. https://doi.org/10.1016/s0733-8635(05)70019-x.

Dhivya, S., Padma, V., Santhini, E., 2015. Wound dressings – a review. BioMed 5, 22. https://doi.org/10.7603/s40681-015-0022-9.

Enoch, S., Leaper, D.J., 2008. Basic science of wound healing. Surgery 28, 31–37. https://doi.org/10.1016/j.mpsur.2007.11.005.

Faccendini, A., Ruggeri, M., Miele, D., Rossi, S., Bonferoni, M.C., Aguzzi, C., Grisoli, P., Viseras, C., Vigani, B., Sandri, G., Ferrari, F., 2020. Norfloxacin-Loaded Electrospun Scaffolds: Montmorillonite Nanocomposite vs. Free Drug. Pharmaceutics. 12 (4), 325. https://doi.org/10.3390/pharmaceutics12040325.

Faccendini, A., Bianchi, E., Ruggeri, M., Vigani, B., Perotti, C., Pavesi, F.C., Caliogna, L., Natali, F., Del Favero, E., Cantu', L., Ferrari, F., Rossi, S., Sandri, G., 2021. Smart Device for Biologically Enhanced Functional Regeneration of Osteo-Tendon Interface. Pharmaceutics. 13 (12), 1996. https://doi.org/10.3390/pharmaceutics13121996.

Fang, K., Wang, R., Zhang, H., Zhou, L., Xu, T., Xiao, Y., Zhou, Y., Gao, G., Chen, J., Liu, D., Ai, F., Fu, J., 2020. Mechano-responsive, tough, and antibacterial zwitterionic hydrogels with controllable drug release for wound healing applications. ACS Appl. Mater. Interfaces 12 (47), 52307–52318.

Florindo, C., Branco, L.C., Marrucho, I.M., 2019. Quest for Green-Solvent Design: From Hydrophilic to Hydrophobic (Deep) Eutectic Solvents. Chem. Sus. Chem. 12 (8), 1549–1559. https://doi.org/10.1002/cssc.201900147.

Frykberg, R.G., Banks, J., 2015. Challenges in the Treatment of Chronic Wounds. Adv Wound Care. 4 (9), 560–582. https://doi.org/10.1089/wound.2015.0635.

Goonoo, N., Jeetah, R., Bhaw-Luximon, A., Jhurry, D., 2015. Polydioxanone-based biomaterials for tissue engineering and drug/gene delivery applications. Eur. J. Pharm. Biopharm. 97, part B, 371–391. https://doi.org/10.1016/j.ejpb.2015.05.024.

Goonoo, N., Fahmi, A., Jonas, U., Gimie, F., Arsa, I.A., Benard, S., Schönherr, H., Bhaw-Luximon, A., 2019. Improved multicellular response, biomimetic mineralization, angiogenesis, and reduced foreign body response of modified polydioxanone scaffolds for skeletal tissue regeneration. ACS Appl. Mater. Interfaces 11 (6), 5834–5850. https://doi.org/10.1021/acsami.8b19929.

Ha, Y.I., Kim, J.H., Park, E.S., 2022. Histological and molecular biological analysis on the reaction of absorbable thread; polydioxanone and polycaprolactone in rat model. J. Cosmet. Dermatol. 21 (7), 2774–2782.

Hansen, B.B., Spittle, S., Chen, B., Poe, D., Zhang, Y., Klein, J.M., Horton, A., Adhikari, L., Zelovich, T., Burcu Gurkan, B.W., Maginn, E.J., Ragauskas, A., Dadmun, M., Zawodzinski, T.A., Baker, G.A., Tuckerman, M.E., Savinell, R.F., Sangoro, J.R., 2020a. Deep eutectic solvents: A review of fundamentals and applications. Chem. Rev. 121 (3), 1232–1285. https://doi.org/10.1021/acs.chemrev.0c00385.

Hansen, B.B., Spittle, S., Chen, B., Poe, D., Zhang, Y., Klein, J.M., Horton, A., Adhikari, L., Zelovich, T., Doherty, B.W., Gurkan, B., Maginn, E.J., Ragauskas, A., Dadmun, M., Zawodzinski, T.A., Baker, G.A., Tuckerman, M.E., Savineli, R.F., Sangoro, J.R., 2020b. Deep eutectic solvents: A review of fundamentals and applications. Chem. Rev. 121 (3), 1232–1285. https://doi.org/10.1021/acs.chemrev.0c00385.

Huang, Q., Wu, T., Wang, L., Zhu, J., Guo, Y., Yu, X., Fan, L., Xin, H.J., Yu, H., 2022. A multifunctional 3D dressing unit based on the core–shell hydrogel microfiber for diabetic foot wound healing. Biomater. Sci. 10 (10), 2568–2576. https://doi.org/10.1039/D2BM00029F.

Jia, Z., Gong, J., Zeng, Y., Ran, J., Liu, J., Wang, K., Xie, C., Lu, X., Wang, J., 2021. Bioinspired conductive silk microfiber integrated bioelectronic for diagnosis and wound healing in diabetes. Adv. Funct. Mater. 31 (19), 2010461. https://doi.org/10.1002/adfm.202010461.

Kang, H.J., Song, Y.S., 2022. Effects of humidity and temperature on hydrolytic degradation of polydioxanone. Polym. Eng. Sci. 62 (6), 2070–2078. https://doi.org/10.1002/pen.25989.

Kim, H.S., Sun, X., Lee, J.H., Kim, H.W., Fu, X., Leong, K.W., 2019. Advanced drug delivery systems and artificial skin grafts for skin wound healing. Adv. Drug Deliv. Rev. 146, 209–239. https://doi.org/10.1016/j.addr.2018.12.014.

Kwon, T.R., Han, S.W., Yeo, I.K., Kim, J.H., Kim, J.M., Hong, J.Y., Lee, B.C., Lee, S.E., Moon, H.S., Kwon, H.J., Kim, B.J., 2019. Biostimulatory effects of polydioxanone, poly-d, l lactic acid, and polycaprolactone fillers in mouse model. J. Cosmet. Dermatol. 18 (4), 1002–1008.

Martins, J.A., Lach, A.A., Morris, H.L., Carr, A.J., Mouthuy, P.A., 2020. Polydioxanone implants: A systematic review on safety and performance in patients. J. Biomater. Appl. 34 (7), 902–916. https://doi.org/10.1177/0885328219888841.

McClure, M.J., Sell, S.A., Ayres, C.E., Simpson, D.G., Bowlin, G.L., 2009. Electrospinning aligned and random polydioxanone-polycaprolactone-silk fibroin blended scaffolds: geometry for a vascular matrix. Biomed. Mater. 4, 055010 https://doi.org/10.1088/1748-6041/4/5/055010.

Mofazzal Jahromi, M.A., Sahandi Zangabad, P., Moosavi Basri, S.M., Sahandi Zangabad, K., Ghamarypour, A., Aref, A.R., Karimi, M., Hamblin, H.R., 2018. Nanomedicine and advanced technologies for burns: Preventing infection and facilitating wound healing. Adv. Drug. Deliv. Rev. 123, 33–64. https://doi.org/10.1016/j.addr.2017.08.001.

Mori, N., Usuki, T., 2022. Extraction of essential oils from tea tree (Melaleuca alternifolia) and lemon grass (Cymbopogon citratus) using betaine-based deep eutectic solvent (DES). PCA. 33 (6), 827–994. https://doi.org/10.1002/pca.3132.

Nikolova, M.P., Chavali, M.S., 2019. Recent advances in biomaterials for 3D scaffolds: A review. Bioact. Mater. 4, 271–292. https://doi.org/10.1016/j.bioactmat.2019.10.005.

Obregon, N., Agubra, V., Pokhrel, M., Campos, H., Flores, D., De la Garza, D., Mao, Y., Macossay, J., Alcoutlabi, M., 2016. Effect of Polymer Concentration, Rotational Speed, and Solvent Mixture on Fiber Formation Using Forcespinning®. Fibers. 4 (2), 20. https://doi.org/10.3390/fib4020020.

Ramphul, H., Bhaw-Luximon, A., Jhurry, D., 2017. Sugar-cane bagasse derived cellulose enhances performance of polylactide and polydioxanone electrospun scaffold for tissue engineering. Carbohydr. Polym. 178, 238–250. https://doi.org/10.1016/j.carbpol.2017.09.046.

Rashid, M., Dudhia, J., Dakin, S.G., Snelling, S.J.B., De Godoy, R., Mouthuy, P.A., Smith, R.K.W., Morrey, M., Carr, A.J., 2020. Histopathological and immunohistochemical evaluation of cellular response to a woven and electrospun polydioxanone (PDO) and polycaprolactone (PCL) patch for tendon repair. Sci. Rep. 10, 4754. https://doi.org/10.1038/s41598-020-61725-5.

Roda, A., Matias, A.A., Paiva, A., Duarte, A.R.C., 2019. Polymer science and engineering using deep eutectic solvents. Polymers 11 (5), 912. https://doi.org/10.3390/polym11050912.

Rowland, D.C., Aquilina, T., Klein, A., Hakimi, O., Alexis-Mouthuy, P., Carr, A.J., Snelling, S.J., 2016-. A comparative evaluation of the effect of polymer chemistry and fiber orientation on mesenchymal stem cell differentiation. J. Biomed. Mater. Res. A. 104 (11), 2843–2853. https://doi.org/10.1002/jbm.a.35829.

Ruggeri, M., Bianchi, E., Rossi, S., Vigani, B., Bonferoni, M.C., Caramella, C., Sandri, G., Ferrari, F., 2020. Nanotechnology-Based medical Devices for the Treatment of Chronic Skin Lesions: From Research to the Clinic. Pharmaceutics 12, 815. https://doi.org/10.3390/pharmaceutics12090815.

Ruggeri, M., Bianchi, E., Rossi, S., Boselli, C., Cornaglia, A.I., Malavasi, L., Carzino, R., Suarato, G., Sánchez-Espejo, R., Athanassiou, A., Viseras, C., Ferrari, F., Sandri, G., 2021. Maltodextrin-amino acids electrospun scaffolds cross-linked with Maillard reaction for skin tissue engineering. Mater. Sci. Eng. C 112593. https://doi.org/10.1016/j.msec.2021.

Sandri, G., Rossi, S., Bonferoni, M.C., Caramella, C., Ferrari, F. Electrospinning Technologies in Wound Dressing Applications. 2020. Chapter 14, In Therapeutic Dressings and Wound Healing Applications. Book Editor: Joshua Boateng 10.1002/9781119433316.ch14.

Sandri, G., Rossi, S., Bonferoni, M.C., Miele, D., Faccendini, A., Del Favero, E., Di Cola, E., Icaro Cornaglia, A., Boselli, C., Luxbacher, T., Malavasi, L., Cantù, L., Ferrari, F., 2019. Chitosan/glycosaminoglycan scaffolds for skin reparation. Carbohydr. Polym. 220, 219–227. https://doi.org/10.1016/j.carbpol.2019.05.069.

Sandri, G., Faccendini, A., Longo, M., Ruggeri, M., Rossi, S., Bonferoni, M.C., Miele, D., Prina-Mello, A., Aguzzi, C., Viseras, C., Ferrari, F., 2020a. Halloysite- and Montmorillonite-Loaded Scaffolds as Enhancers of Chronic Wound Healing. Pharmaceutics. 12 (2), 179. https://doi.org/10.3390/pharmaceutics12020179.

Saska, S., Pilatti, L., Silva, E.S.d.S., Nagasawa, M.A., Câmara, D., Lizier, N., Finger, E., Dyszkiewicz Konwińska, M., Kempisty, B., Tunchel, S., Blay, A., Shibli, J.A., 2021. Polydioxanone-Based Membranes for Bone Regeneration. Polymers. 13, 1685. https://doi.org/10.3390/polym13111685.

Shafie, M.H., Yusof, R., Gan, C.Y., 2019. Synthesis of citric acid monohydrate-choline chloride based deep eutectic solvents (DES) and characterization of their physicochemical properties. J. Mol. Liq. 288, 111081 https://doi.org/10.1016/j.molliq.2019.111081.

Singer, A.J., Clark, R.A., 1999. Cutaneous wound healing. NEJM 341 (10), 738–746. https://doi.org/10.1056/NEJM199909023411006.

Song, S.J., Shin, Y.C., Kim, S.E., Kwon, I.K., Lee, J.H., Hyon, S.H., Han, D.W., Kim, B., 2018. Aligned laminin core-polydioxanone/collagen shell fiber matrices effective for neuritogenesis. Sci. Rep. 8 (1), 1–11. https://doi.org/10.1038/s41598-018-23958-3.

Wada, A., Kubota, H., Akiyama, T., Hatanaka, H., Miura, H., Iwamoto, Y., 2001. Effect of absorbable polydioxanone flexor tendon repair and restricted active mobilization in a canine model. J. Hand Surg. 26 (3), 398–406.

Wang, C., Chu, C., Zhao, X., Yang, Y., Hu, C., Liu, L., Li, J., Qu, Y., Man, Y., 2022. The diameter factor of aligned membranes facilitates wound healing by promoting epithelialization in an immune way. Bioact. Mater. 11, 206–217. https://doi.org/10.1016/j.bioactmat.2021.09.022.

Wilkinson, H.N., Hardman, M.J., 2020. Wound healing: cellular mechanisms and pathological outcomes. Open Biol. 10 (9), 200223 https://doi.org/10.1098/rsob.200223.

Xu, F., Wang, S., Cao, C., Ma, W., Zhang, X., Du, J., Sun, W., Ma, Q., 2022. Microfluidic generation of multifunctional core-shell microfibers promote wound healing. Colloids Surf. B 219, 112842. https://doi.org/10.1016/j.colsurfb.2022.112842.

Yue, H., Zhou, L., Zou, R., Li, Z., Liao, T., Yan, J., Zhou, Y., Yang, M., Piao, Z., 2019. Promotion of skin fibroblasts collagen synthesis by polydioxanone mats combined with concentrated growth factor extracts. J. Biomater. Appl. 34 (4), 487–497. https://doi.org/10.1177/0885328219858456.

Zhang, W., Shen, J., Gao, P., Jiang, Q., Xia, W., 2022. Sustainable chitosan films containing a betaine-based deep eutectic solvent and lignin: Physicochemical, antioxidant, and antimicrobial properties. FoodHydrocoll. 129, 107656 https://doi.org/10.1016/j.foodhyd.2022.107656.

Zhou, X., Pan, Y., Liu, R., Luo, X., Zeng, X., Zhi, D., Li, J., Cheng, Q., Huang, Z., Zhang, H., Wang, K., 2019. Biocompatibility and biodegradation properties of polycaprolactone/polydioxanone composite scaffolds prepared by blend or co-electrospinning. J. Bioact. Compat. Polym. 34 (2), 115–130. https://doi.org/10.1177/0883911519835569.